

Supporting Information

A Cobalt Molecular Catalyst for Hydrogen Evolution Reaction with Remarkable Activity in Phosphate Buffered Water Solution

Caterina Trotta,^a Pardeep Dahiya,^b Lorenzo Baldinelli,^a Gabriel Menendez Rodriguez,^{*a} Priyanka Chakraborty,^b Giovanni Bistoni,^{*a} Filippo De Angelis,^a Basker Sundararaju,^{*b} and Alceo Macchioni.^{*a}

^a Department of Chemistry, Biology and Biotechnology, Università degli Studi di Perugia, Via Elce di Sotto 8, 06123-Perugia, Italy

^b Department of Chemistry, Indian Institute of Technology Kanpur, Uttar Pradesh, - 208 016 Kanpur, India.

E-mail: gabriel.menendezrodriguez@unipg.it; giovanni.bistoni@unipg.it; basker@iitk.ac.in;
alceo.macchioni@unipg.it

Contents

I. Experimental	3
General information.....	3
Synthesis and characterization.....	3
Electrochemistry	4
RRDE experiments.....	4
Faradaic efficiency.....	5
II. Electrochemical experiments	6
Cyclic and square wave voltammograms	6
RRDE and faradaic efficiency.....	9
Catalyst stability and rinse test.....	11
Overpotential determination.....	13
Turnover frequency of 1-4	14
Effect of catalyst concentration.....	16
Effect of pH.....	18
Effect of phosphate buffer concentration	19
III. DFT calculations	20
The interaction between the catalyst and the buffer.....	21
First reduction peak and catalyst activation.....	22
Metal-hydride complex formation and predicted overpotentials	22
Hydrogen evolution and the origin of TOF	23
Computational details	24
References	25

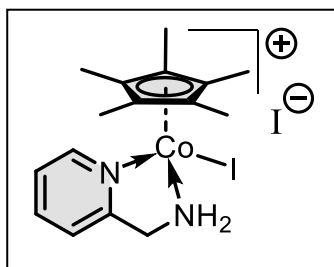
I. Experimental

General information

All solvents and reagents were purchased from SIGMA-ALDRICH and used without any further purification. Distilled water was further purified using a Milli-Q Ultrapure water purification system. Phosphate buffer solutions were prepared by mixing different volumes of previously prepared acid and base stock solutions.

Synthesis and characterization

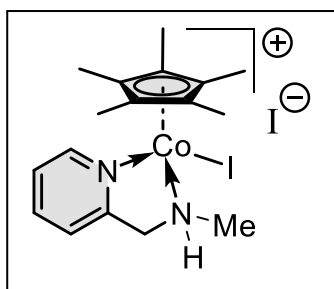
Complex 1: An oven-dried Schlenk tube equipped with a magnetic stir bar was charged with



[Cp*Co(CO)I₂] (100 mg, 0.211 mmol, 1.0 equiv.), pyridin-2-ylmethanamine (23 mg, 0.211 mmol, 1.0 equiv.) and 5 mL DCM under Argon atmosphere. The resultant reaction mixture under argon in a closed Schlenk tube was stirred at room temperature for 24 hours. After which the solution was filtered through a pad of celite. The filtrate was concentrated under vacuum to give a black-green solid. The crude solid

was further purified by column chromatography using silica gel as a stationary phase and eluted with 10% MeOH/DCM to give the product as a black-green solid in 59% (69 mg) yield. ¹H NMR (400 MHz, CDCl₃): δ 9.04 (d, *J*=5.29 Hz, 1H), 7.82 (t, *J*=7.37 Hz, 1H), 7.56 (t, *J*=7.10 Hz, 1H), 7.36 (d, *J*=9.01 Hz, 1H), 6.34 (s, 1H), 4.76-4.69 (m, 1H), 3.99 (dd, *J*=17.29, 6.38 Hz, 1H), 2.96-2.87 (m, 1H), 1.76 (s, 15H). ¹³C {¹H} NMR (100 MHz, CDCl₃): δ 162.2, 154.6, 139.1, 125.6, 121.6, 93.8, 51.3, 11.6. HRMS: Calculated for C₁₆H₂₃CoI₂N₂ is [M-I]⁺ 429.0233; found 429.0238. CHN: Anal. Calcd. for C₁₆H₂₃CoI₂N₂: C, 34.56%; H, 4.17%; N, 5.04%; others, 56.23%. Found: C, 33.88%; H, 4.01%; N, 5.63%, others, 56.48%. IR (cm⁻¹): 3187, 3119, 2908, 1608, 1426, 1378, 1271, 1137, 1102, 1005, 939, 775, 467, 418. X-ray Crystal Structure: CCDC 1939352 data can be obtained free of charge from the Cambridge Crystallographic Data Centre.

Complex 2: An oven-dried Schlenk tube equipped with a magnetic stir bar was charged with



[Cp*Co(CO)I₂] (100 mg, 0.211 mmol, 1.0 equiv.), N-methyl-1-(pyridin-2-yl)methanamine (23 mg, 0.211 mmol, 1.0 equiv.) and 5 mL DCM under Argon atmosphere. The resultant reaction mixture under argon in a closed Schlenk tube was stirred at room temperature for 12 hours. After which the solution was filtered through a pad of celite. The filtrate was concentrated under vacuum to give a dark-green solid. The crude solid

was further purified by column chromatography using silica gel as a stationary phase and eluted with 10% MeOH/DCM to give the product as a dark-green solid in 37% (44 mg) yield. ¹H NMR (400 MHz, CDCl₃): δ 9.08 (d, *J* = 5.7 Hz, 1H), 7.76 (d, *J* = 6.5 Hz, 1H), 7.47

(t, $J = 6.5$ Hz, 1H), 7.47 (t, $J = 6.5$ Hz, 1H), 7.22 (d, $J = 7.9$ Hz, 1H), 7.14 (s, 1H), 4.57 (s, 1H), 2.97 (dd, $J = 15.7, 8.9$ Hz, 1H), 2.91 (d, $J = 5.9$ Hz, 3H), 1.80 (s, 15H). ^{13}C $\{^1\text{H}\}$ NMR (100 MHz, CDCl_3): δ 162.7, 152.3, 138.8, 125.1, 121.4, 93.5, 61.1, 43.8, 29.6, 11.6 HRMS: Calculated for $\text{C}_{17}\text{H}_{25}\text{CoI}_2\text{N}_2$ is $[\text{M-I}]^+$ 443.0394; found 443.0386. IR (cm^{-1}): 3241, 2958, 2920, 1609, 1478, 1430, 1376, 1261, 1155, 1018, 944, 765, 733. X-ray Crystal Structure: CCDC 2297771 data can be obtained free of charge from the Cambridge Crystallographic Data Centre.

Electrochemistry

Electrochemical measurements were carried out at room temperature under an atmosphere of nitrogen using a Squidstat Plus potentiostat (manufactured by Admiral Instruments). In all experiments, a classical three-electrode electrochemical cell with a capacity of 20.0 mL equipped with a Hg/HgSO_4 (Sat'd K_2SO_4) reference electrode, a platinum wire as the counter electrode and a 3 mm glassy carbon working electrode (CH Instruments) was used. No iR -correction was applied. Potentials in aqueous solutions were referenced to the normal hydrogen electrode (NHE) using the formula $E_{\text{NHE}} = E_{\text{Hg}/\text{HgSO}_4}^\circ + E_{\text{Hg}/\text{HgSO}_4}$, where $E_{\text{Hg}/\text{HgSO}_4}^\circ = +0.65$ V. Between each electrochemical experiment the surface of the working electrode was mechanically polished with 0.05 micron alumina for 15-20 seconds, thoroughly rinsed with ultrapure water and gently polished with a Kimwipe to remove the water from the surface. Square Wave Voltammetry experiments were performed with a potential step of 1 mV, a pulse amplitude of 10 mV and a frequency of 10 Hz. Controlled potential electrolysis (CPE) experiments were performed at -1.35 V vs. NHE under controlled stirring (5000 rpm) and nitrogen atmosphere on a 200 μM solution of **1-4**. A standard two-compartment H-cell equipped with a glassy carbon working electrode (Area = 0.071 cm^2), a Hg/HgSO_4 (Sat'd K_2SO_4) reference electrode and a platinum coil as the counter electrode separated from the cell solution by a Vycor frit was used.

RRDE experiments

RRDE experiments were performed with RRDE-3A rotating ring/disk electrode apparatus (ALS, Japan) equipped with a GC disk – Pt ring electrode ($d_1 = 4$ mm, $d_2 = 5$ mm, $d_3 = 7$ mm). All experiments were carried out at 1600 RPM in PBS pH 7 0.1 M after careful deoxygenation with pure nitrogen. Potential values are reported vs. NHE.

The collection efficiency for hydrogen (N) was determined by generating H_2 on the GC disk coated with Pt on graphitized carbon¹ (Sigma Aldrich), while keeping the Pt ring at a constant potential where H_2 oxidation occurs.²⁻⁴ In particular, the disk potential was first held constant at 0.15 V for 60 seconds, followed by a potential step to -0.55 V for another 60 seconds (Figure S1 left). To enable the detection of the generated hydrogen on the disk, the Pt ring potential was kept constant at -0.15 V. N was calculated by averaging the values of i_{ring} over i_{disk} during the 60 seconds while $E_{\text{disk}} = -0.55$ V (Figure S1 right). The obtained value of N was 0.25, which was used for further calculations.

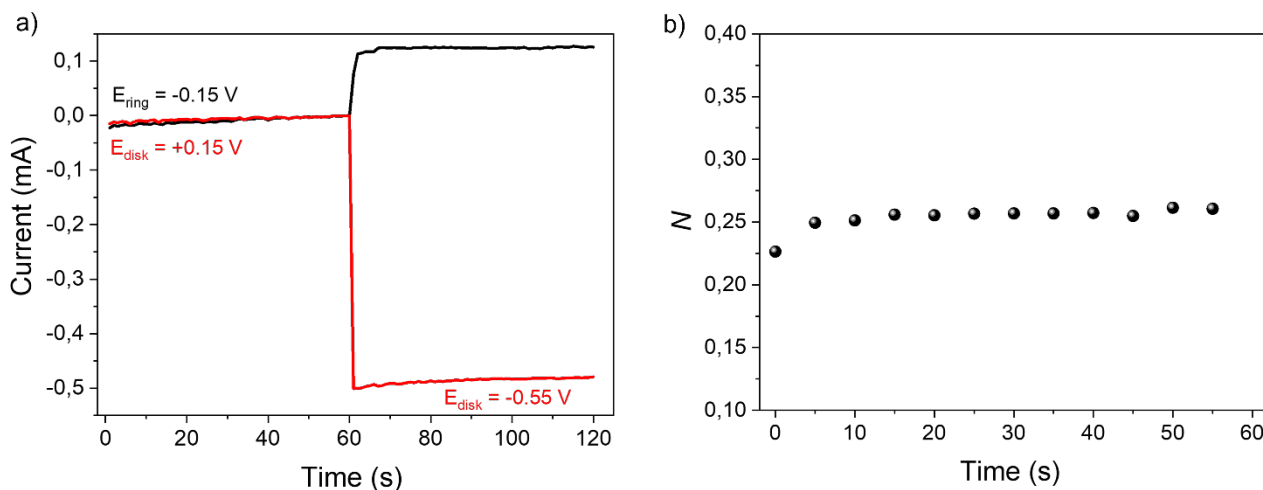


Figure S1. a) Ring current (black) during chronoamperometry at -0.15 V and disk current (red) during stepped voltage (+0.15 to -0.55 V with step length = 60 s). (b) Collection efficiency for H_2 at $E_{\text{disk}} = -0.55 \text{ V}$.

Faradaic efficiency

The faradaic efficiency (FE) of **1-4** was determined using similar RRDE measurements as described in the previous section. First, the disk potential was held at 0.15 V for 60 seconds, followed by a potential step to -1.35 V for another 60 seconds. While the Pt ring potential was kept constant at -0.15 V. The resulting current-response graphs are shown in Figures S2-S5. The faradaic efficiency (FE) of **1-4** was calculated according to the following equation:

$$FE(\%) = \frac{i_R}{i_D \cdot N} \times 100 \quad (1)$$

II. Electrochemical experiments

Cyclic and square wave voltammograms

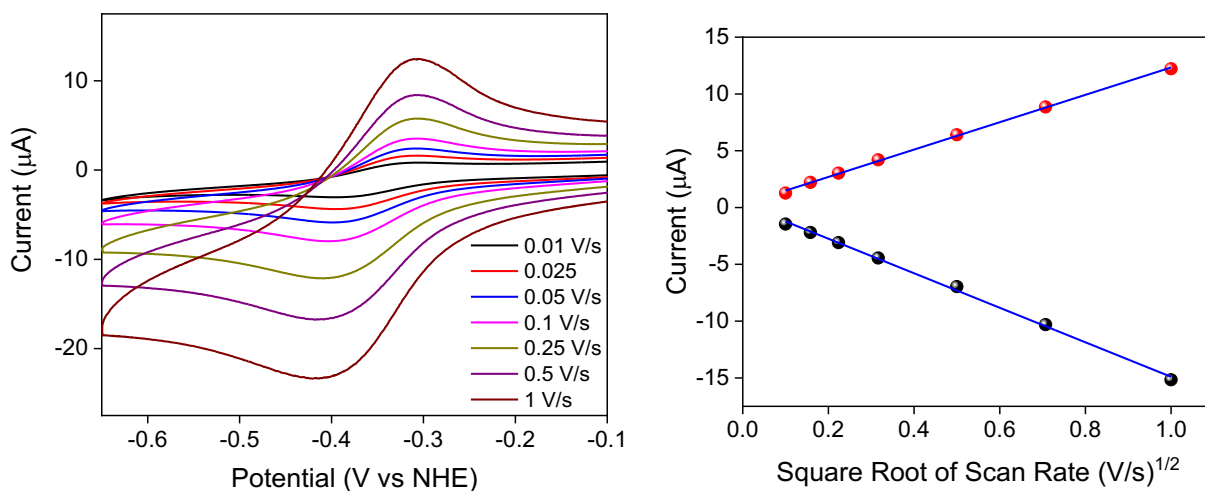


Figure S2. Left) Cyclic voltammograms of **1** (500 μM) at varying scan rates. Right) Plot of the anodic (red dots) and cathodic (black dots) peak currents of **1** as a function of the square root of the scan rate. Conditions: 0.1 M PBS pH 7, N_2 atmosphere, 298 K.

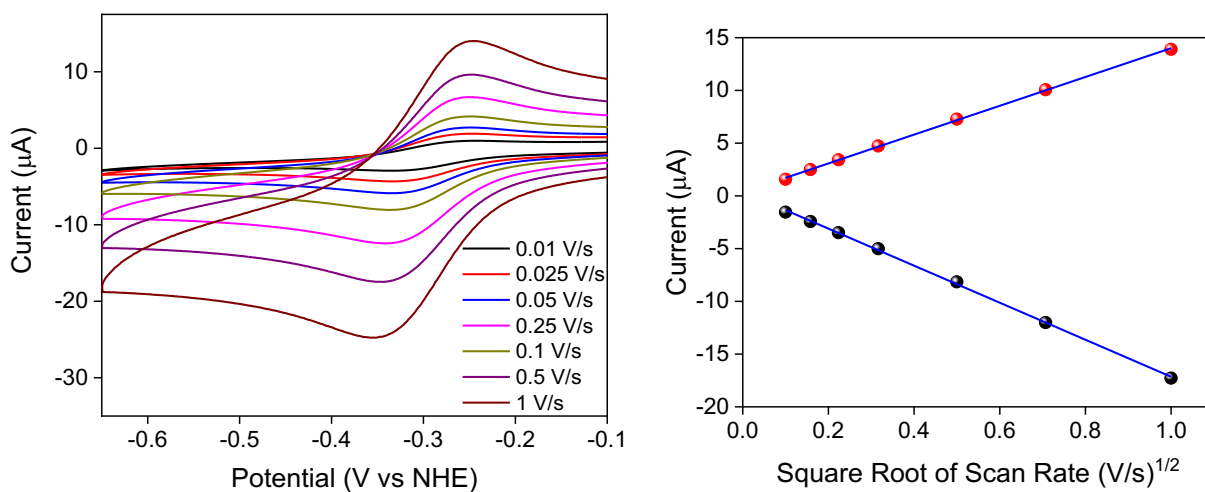


Figure S3. Left) Cyclic voltammograms of **2** (500 μM) at varying scan rates. Right) Plot of the anodic (red dots) and cathodic (black dots) peak currents of **2** as a function of the square root of the scan rate. Conditions: 0.1 M PBS pH 7, N_2 atmosphere, 298 K.

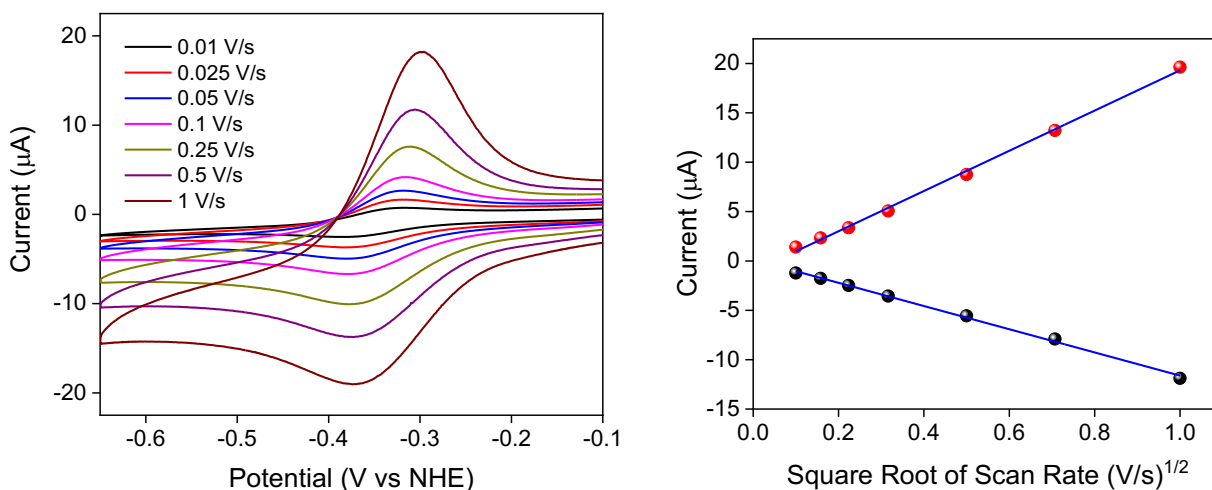


Figure S4. Left) Cyclic voltammograms of **3** (500 μM) at varying scan rates. Right) Plot of the anodic (red dots) and cathodic (black dots) peak currents of **3** as a function of the square root of the scan rate. Conditions: 0.1 M PBS pH 7, N₂ atmosphere, 298 K.

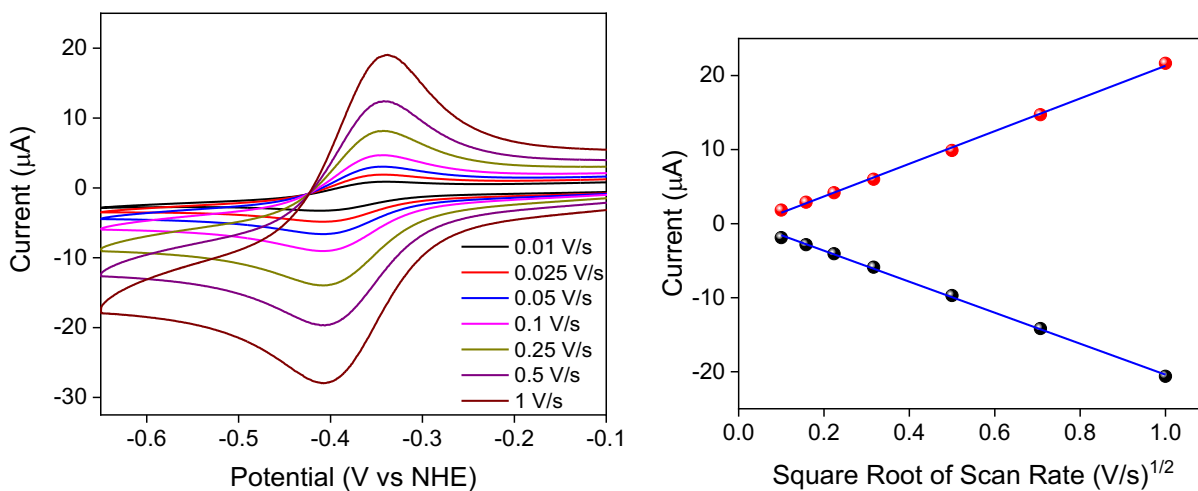


Figure S5. Left) Cyclic voltammograms of **4** (500 μM) at varying scan rates. Right) Plot of the anodic (red dots) and cathodic (black dots) peak currents of **4** as a function of the square root of the scan rate. Conditions: 0.1 M PBS pH 7, N₂ atmosphere, 298 K.

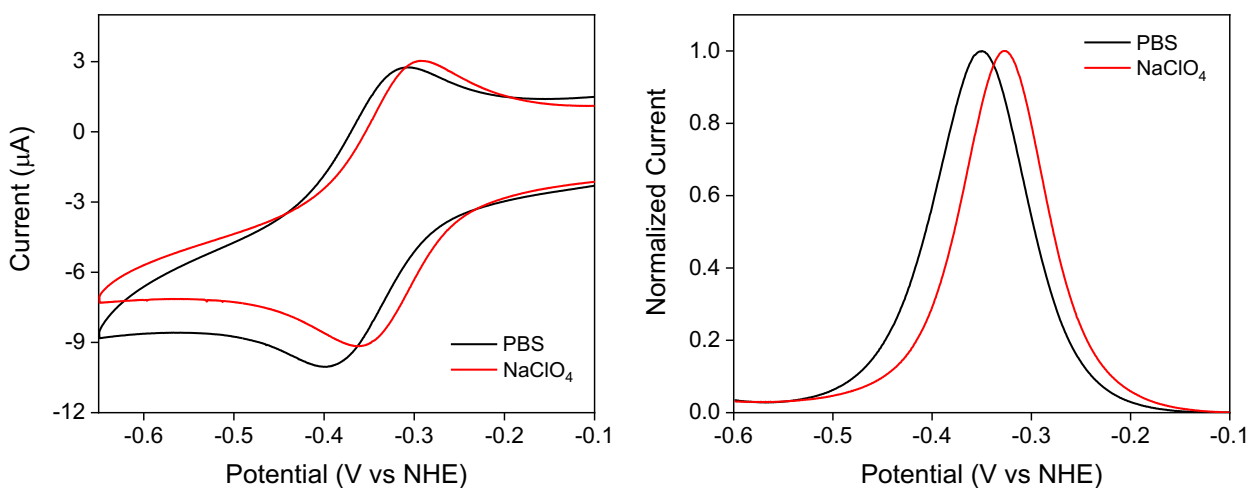


Figure S6. Left) Cyclic voltammograms of **1** (500 μM) at 100 mV/s using PBS pH 7 (black trace) and NaClO_4 (red trace) as supporting electrolyte. Right) Square wave voltammograms of **1** (500 μM) using PBS pH 7 (black trace) and NaClO_4 (red trace) as supporting electrolyte. Conditions: 0.1 M PBS pH 7 or NaClO_4 , N_2 atmosphere, 298 K.

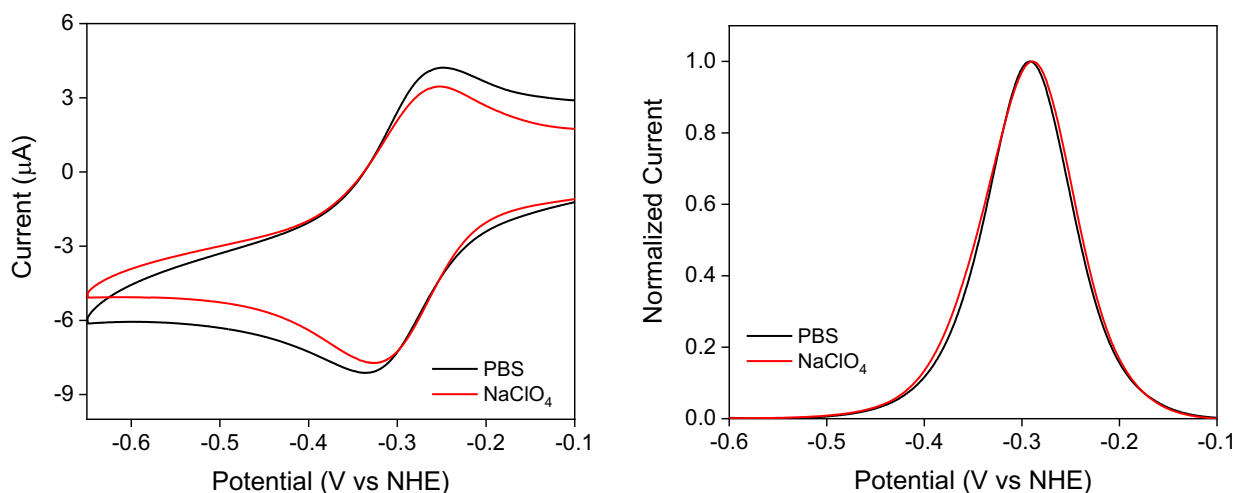


Figure S7. Left) Cyclic voltammograms of **2** (500 μM) at 100 mV/s using PBS pH 7 (black trace) and NaClO_4 (red trace) as supporting electrolyte. Right) Square wave voltammograms of **2** (500 μM) using PBS pH 7 (black trace) and NaClO_4 (red trace) as supporting electrolyte. Conditions: 0.1 M PBS pH 7 or NaClO_4 , N_2 atmosphere, 298 K.

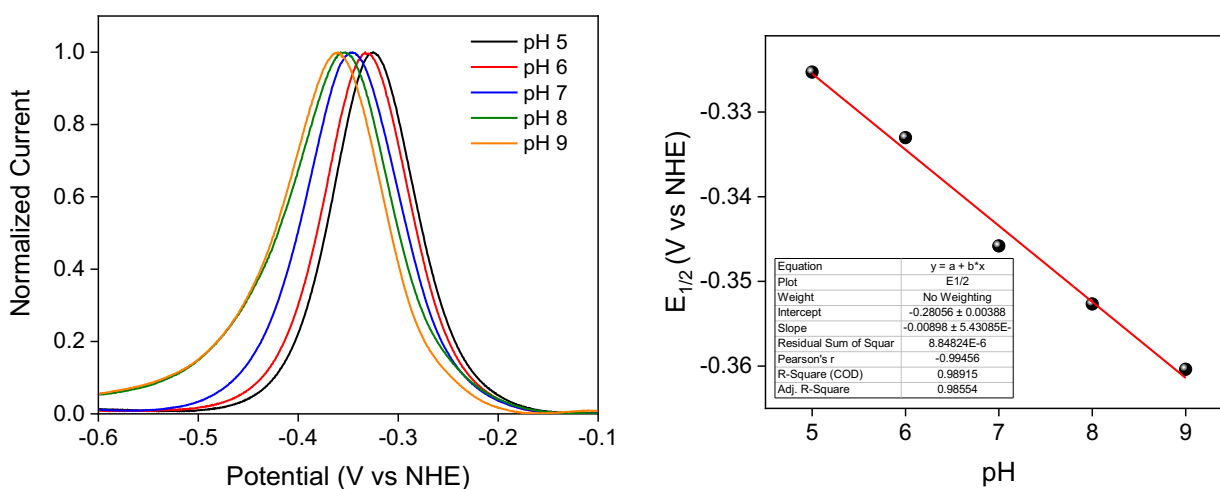


Figure S8. Left) Square wave voltammograms of **1** (500 μM) at varying pH values. Right) Plot of $E_{1/2}$ values of **1** as a function of pH. Conditions: 0.1 M PBS, N_2 atmosphere, 298 K.

RRDE and faradaic efficiency

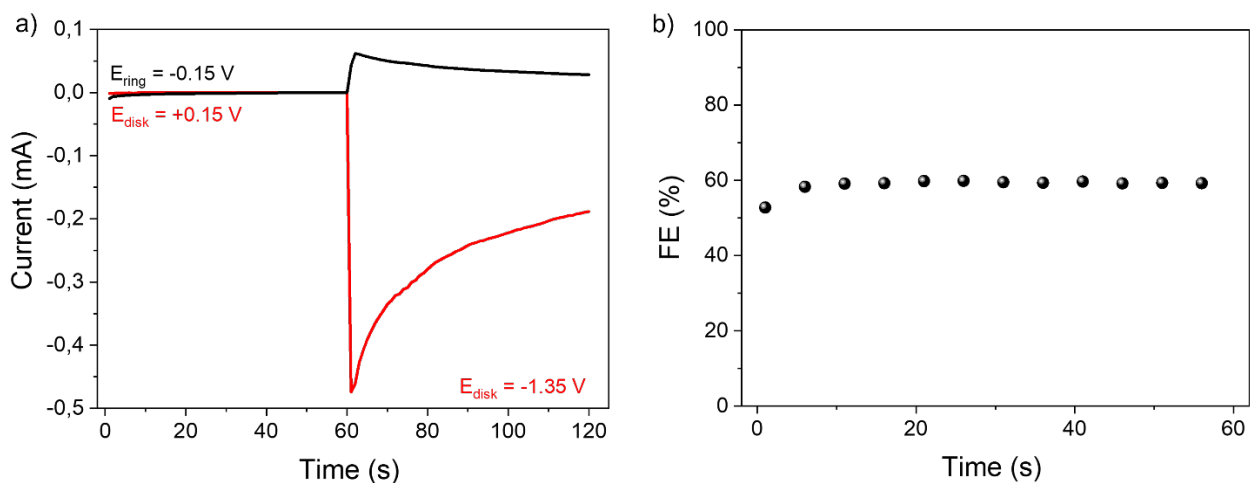


Figure S9. a) Ring current (black) during chronoamperometry at -0.15 V and disk current (red) during stepped voltage (+0.15 to -0.55 V with step length = 60 s). (b) Collection efficiency for H_2 at $E_{\text{disk}} = -1.35$ V. Conditions: [1] = 200 μM , 0.1 M PBS pH 7, N_2 atmosphere, 298 K.

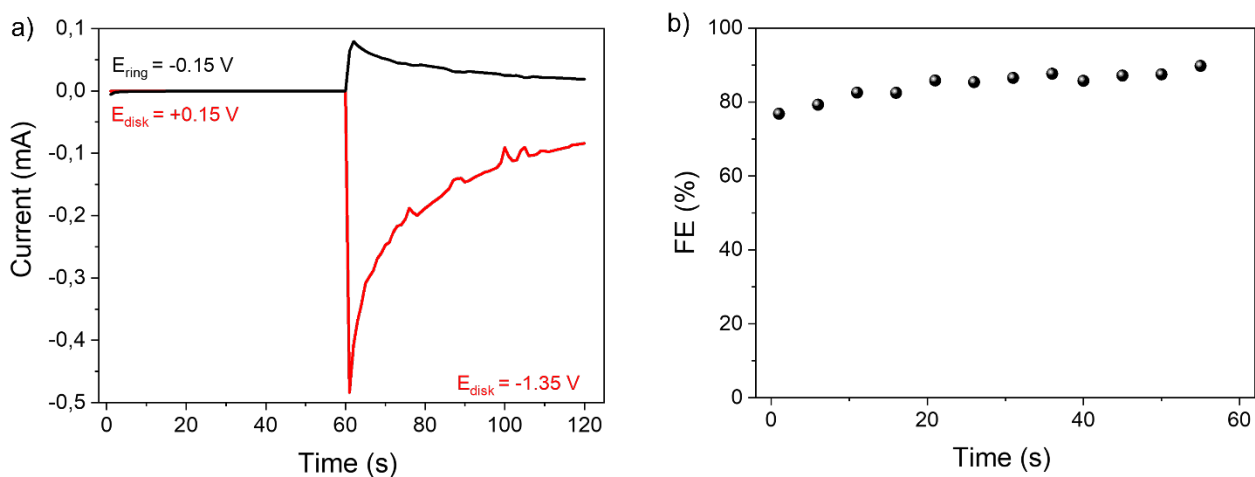


Figure S10. a) Ring current (black) during chronoamperometry at -0.15 V and disk current (red) during stepped voltage (+0.15 to -0.55 V with step length = 60 s). (b) Collection efficiency for H_2 at $E_{\text{disk}} = -1.35$ V. Conditions: [2] = 200 μM , 0.1 M PBS pH 7, N_2 atmosphere, 298 K.

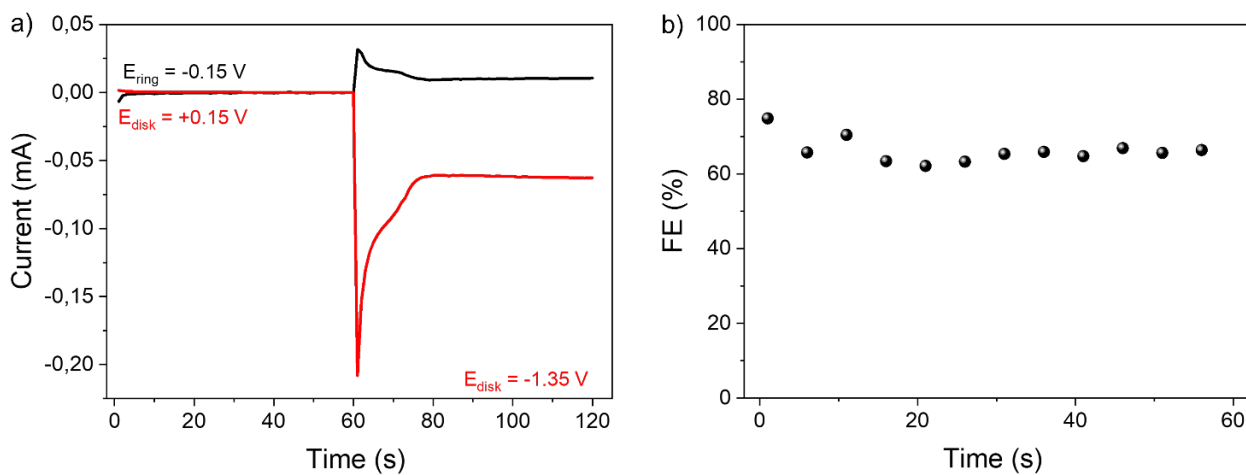


Figure S11. a) Ring current (black) during chronoamperometry at -0.15 V and disk current (red) during stepped voltage (+0.15 to -0.55 V with step length = 60 s). (b) Collection efficiency for H₂ at E_{disk} = -1.35 V. Conditions: [3] = 200 μM, 0.1 M PBS pH 7, N₂ atmosphere, 298 K.

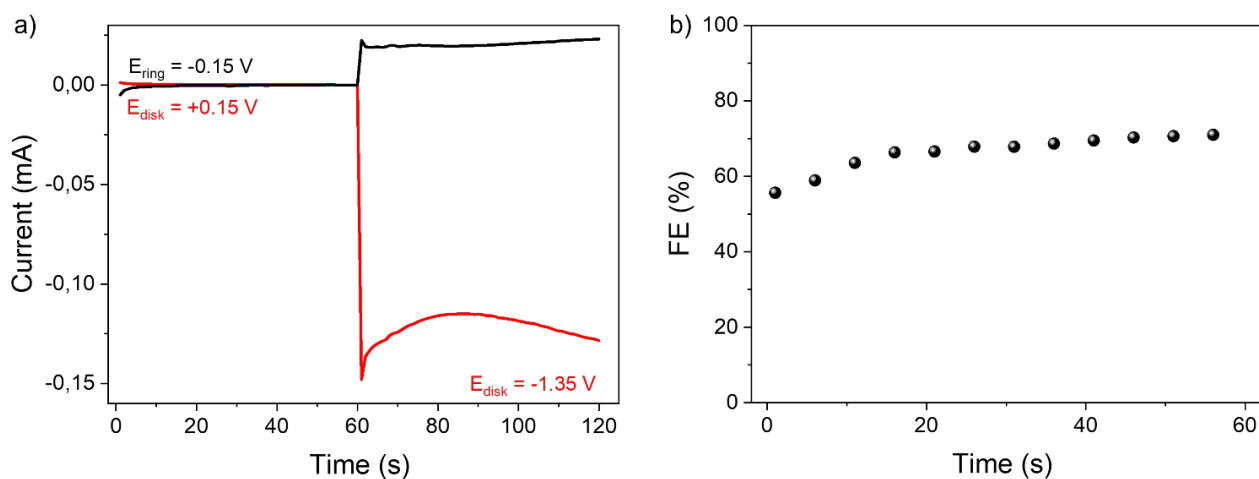


Figure S12. a) Ring current (black) during chronoamperometry at -0.15 V and disk current (red) during stepped voltage (+0.15 to -0.55 V with step length = 60 s). (b) Collection efficiency for H₂ at E_{disk} = -1.35 V. Conditions: [4] = 200 μM, 0.1 M PBS pH 7, N₂ atmosphere, 298 K.

Catalyst stability and rinse test

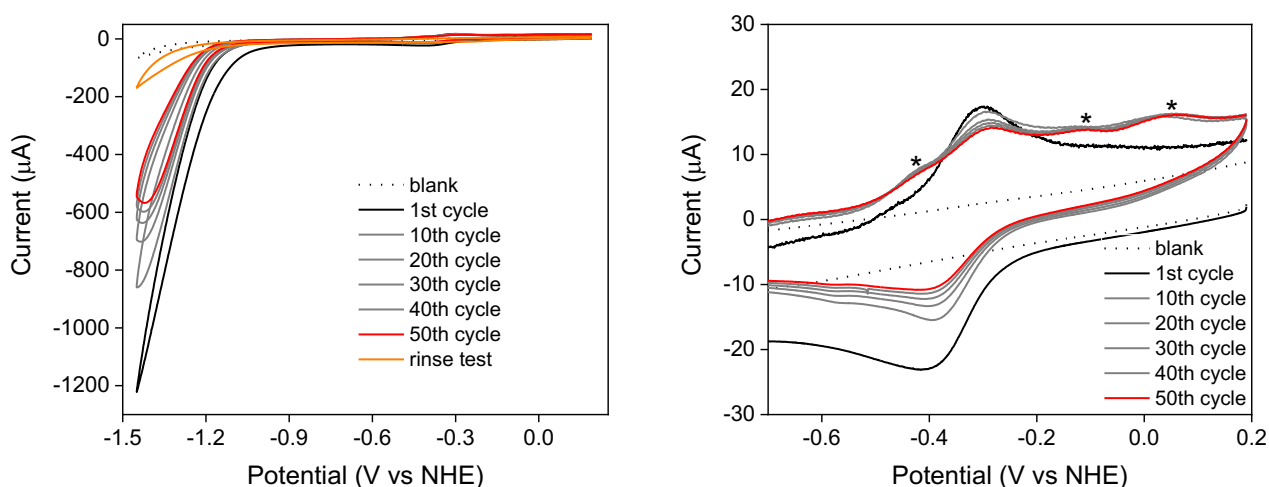


Figure S13. Left) Consecutive cyclic voltammograms of **1** (500 μM) recorded at 1 V/s between 0.19 and -1.45 V vs. NHE. Right) Enlargement from 0.2 to -0.7 V vs NHE that shows the new oxidative features (marked with asterisk) that appear upon cycling the electrode. Conditions: 0.1 M PBS, N₂ atmosphere, 298 K.

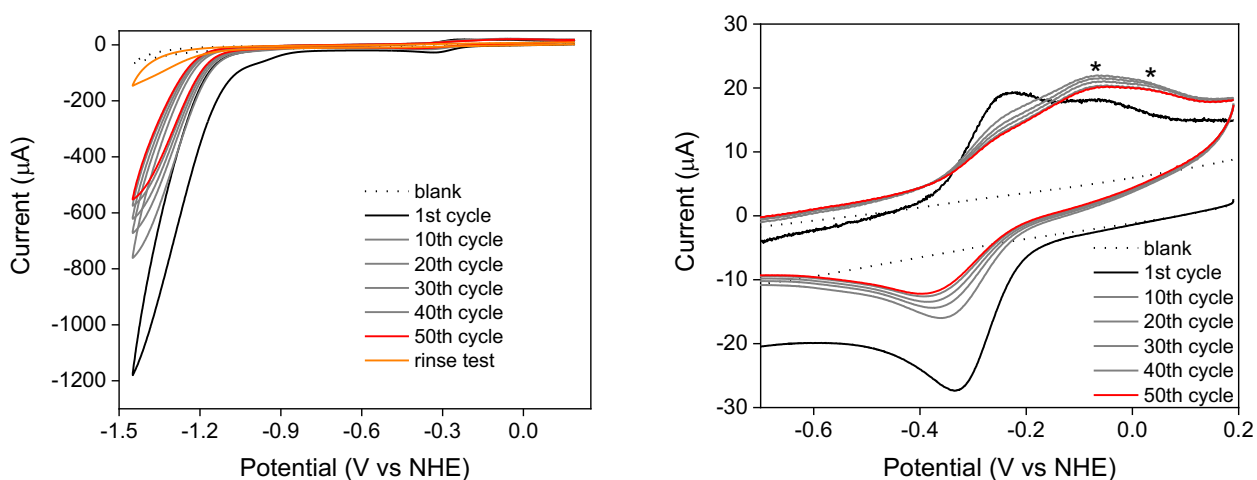


Figure S14. Left) Consecutive cyclic voltammograms of **2** (500 μM) recorded at 1 V/s between 0.19 and -1.45 V vs. NHE. Right) Enlargement from 0.2 to -0.7 V vs NHE that shows the new oxidative features (marked with asterisk) that appear upon cycling the electrode. Conditions: 0.1 M PBS, N₂ atmosphere, 298 K.

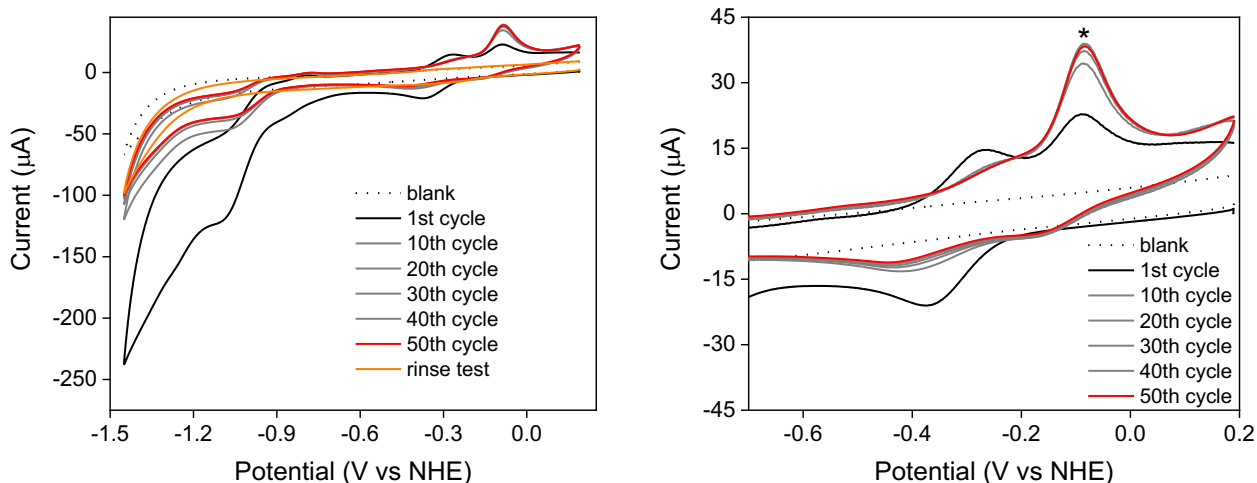


Figure S15. Left) Consecutive cyclic voltammograms of **3** ($500\ \mu\text{M}$) recorded at $1\ \text{V/s}$ between 0.19 and $-1.45\ \text{V}$ vs. NHE. Right) Enlargement from 0.2 to $-0.7\ \text{V}$ vs NHE that shows the new oxidative features (marked with asterisk) that appear upon cycling the electrode. Conditions: $0.1\ \text{M}$ PBS, N_2 atmosphere, $298\ \text{K}$.

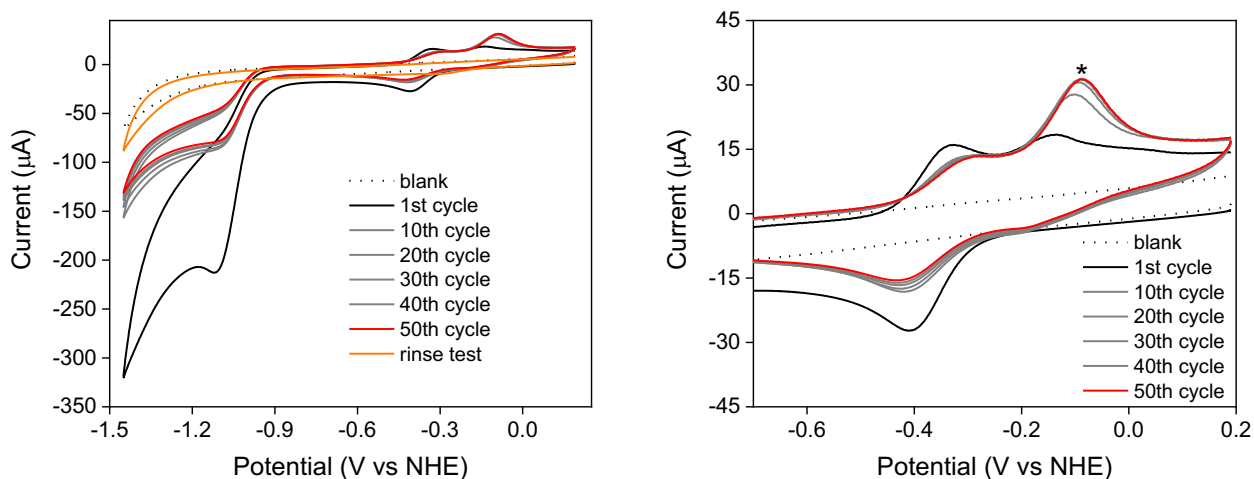


Figure S16. Left) Consecutive cyclic voltammograms of **4** ($500\ \mu\text{M}$) recorded at $1\ \text{V/s}$ between 0.19 and $-1.45\ \text{V}$ vs. NHE. Right) Enlargement from 0.2 to $-0.7\ \text{V}$ vs NHE that shows the new oxidative features (marked with asterisk) that appear upon cycling the electrode. Conditions: $0.1\ \text{M}$ PBS, N_2 atmosphere, $298\ \text{K}$.

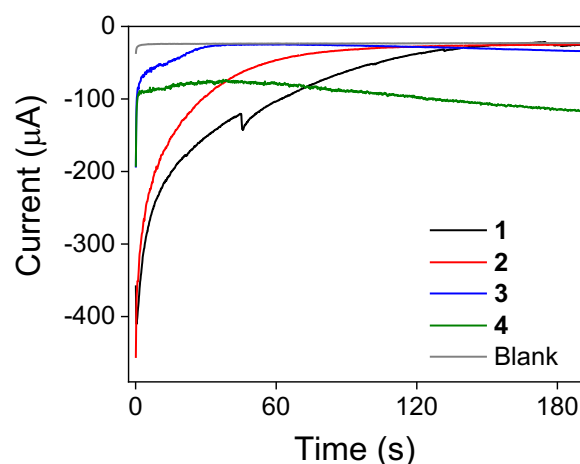


Figure S17. Controlled-potential electrolysis at -1.35 V vs. NHE in the absence (grey line) and in the presence of **1-4** (200 μM). Conditions: 0.1 M PBS, N_2 atmosphere, 298 K.

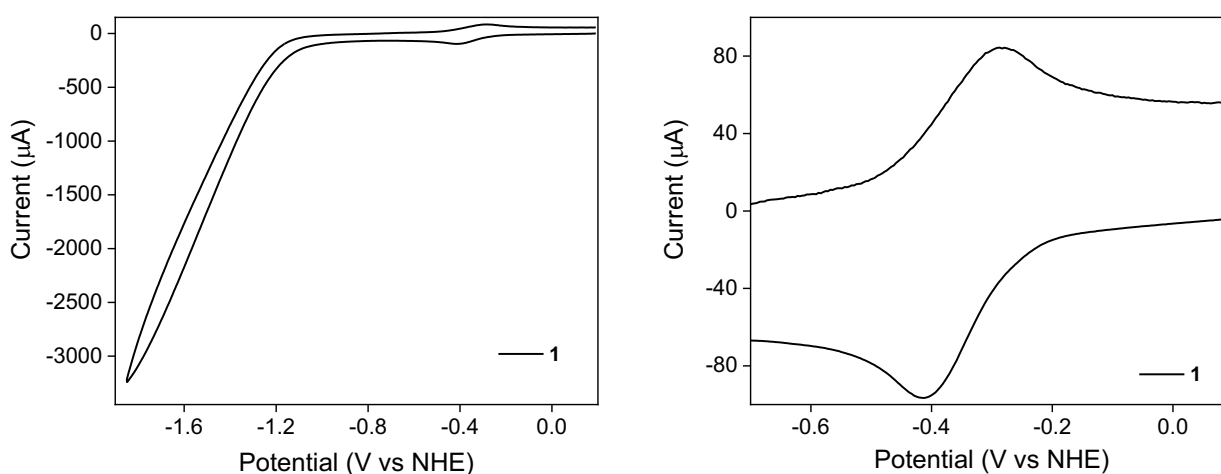


Figure S18. Left) Cyclic voltammogram of **1** (500 μM) recorded at 10 V/s between 0.19 and -1.85 V vs. NHE. Right) Enlarged view of $\text{Co}^{\text{III/II}}$ redox region showing the absence of any additional redox feature. Conditions: 0.1 M PBS, N_2 atmosphere, 298 K.

Overpotential determination

The HER overpotential, $\eta(E_{\text{cat}/2})$,^{5,6} of **1-4** was calculated using Equation 2:

$$\eta(E_{\text{cat}/2}) = E^\circ(2\text{H}^+/\text{H}_2) - E_{\text{cat}/2} \quad (2)$$

Where $E^\circ(2\text{H}^+/\text{H}_2)$ is the standard electrode potential for HER and $E_{\text{cat}/2}$ is the potential at which the catalytic current becomes exactly the half of the maximum catalytic current (Figure S17).

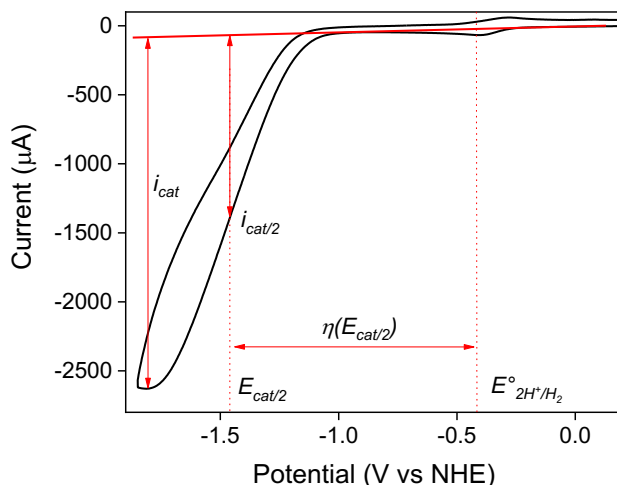


Figure S19. Cyclic voltammogram of **1** (500 μM) recorded at 6 V/s between 0.19 and -1.85 V vs. NHE. $\eta(E_{\text{cat}/2})$ is determined as illustrated in the figure.

Turnover frequency of **1-4**

TOF values of **1-4** were determined using an approximate model for pseudo-first-order catalytic systems (Equation 3):^{7,8}

$$\frac{i_{\text{cat}}}{i_d} = \frac{n_{\text{cat}}}{0.4463} \sqrt{\frac{RT}{Fv n_d^3}} \sqrt{k_{\text{obs}}} \quad (3)$$

where $n_{\text{cat}} = 2$ is the stoichiometric factor for the number of electrons in HER, n_d is the number of electrons involved in the reversible electron transfer process ($n_d = 1$ for the $\text{Co}^{\text{III}}/\text{Co}^{\text{II}}$ redox couple), n is the scan rate, F is the Faraday constant, T is the temperature in Kelvin and R is the ideal gas constant. The plot of i_{cat}/i_d vs $n^{-1/2}$, under the condition where i_{cat} is independent of scan rate, provides a straight line, the slope of which gives immediate access to k_{obs} (or TOF).

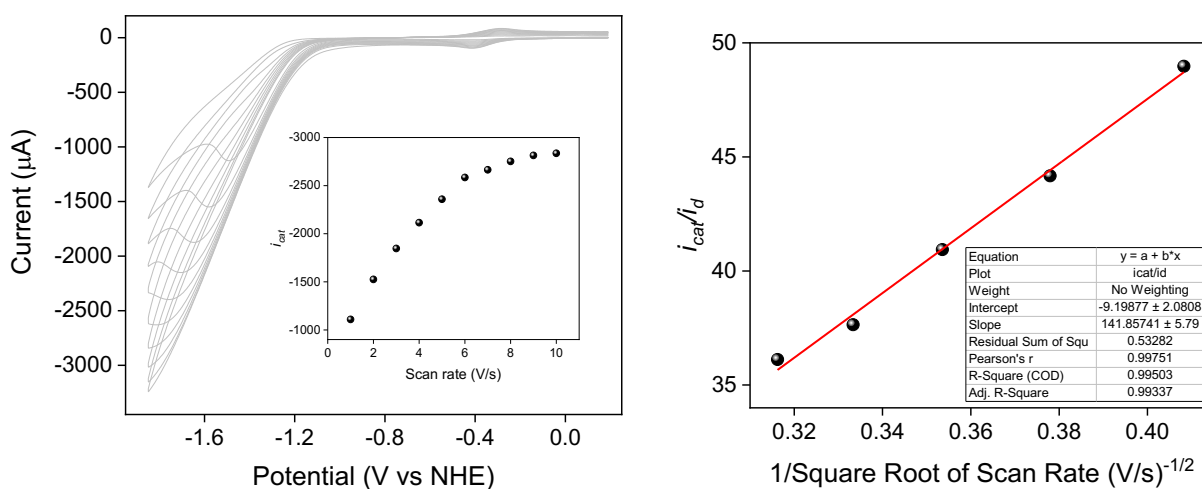


Figure S20. Right) CVs of **1** (500 μM) at various scan rates from 1 to 10 V/s in 0.1 M PBS at pH 7

under N_2 . Inset: plot of i_{cat} versus scan rate. b) Plot of i_{cat}/i_d versus the reciprocal of the square root of scan rate (from 6 to 10 V/s).

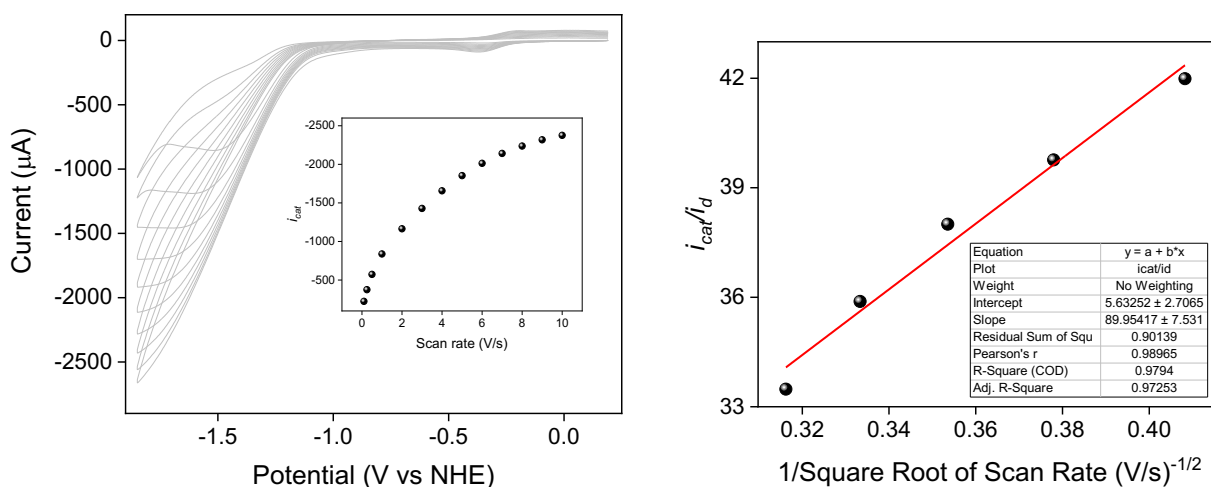


Figure S21. Right) CVs of **2** (500 μM) at various scan rates from 1 to 10 V/s in 0.1 M PBS at pH 7 under N_2 . Inset: plot of i_{cat} versus scan rate. b) Plot of i_{cat}/i_d versus the reciprocal of the square root of scan rate (from 6 to 10 V/s).

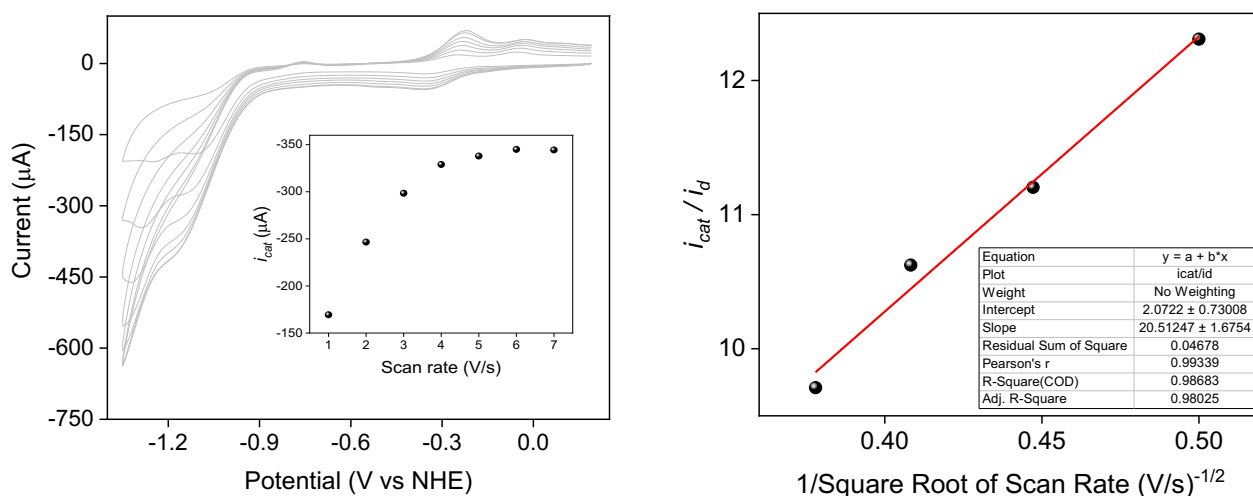


Figure S22. Right) CVs of **3** (500 μM) at various scan rates from 1 to 7 V/s in 0.1 M PBS at pH 7 under N_2 . Inset: plot of i_{cat} versus scan rate. b) Plot of i_{cat}/i_d versus the reciprocal of the square root of scan rate (from 4 to 7 V/s).

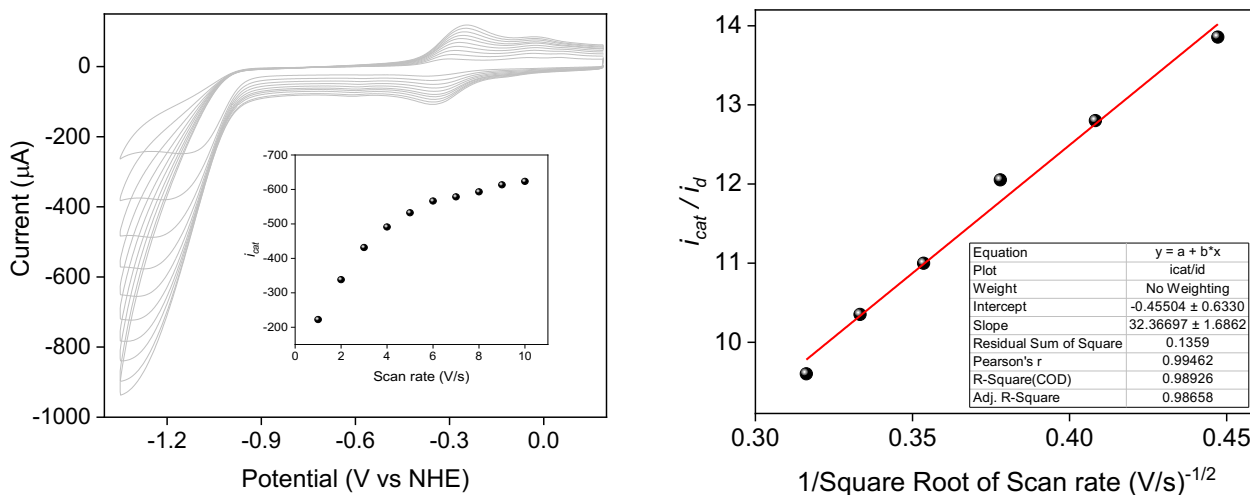


Figure S23. Right) CVs of **4** (500 μM) at various scan rates from 1 to 10 V/s in 0.1 M PBS at pH 7 under N_2 . Inset: plot of i_{cat} versus scan rate. b) Plot of i_{cat}/i_d versus the reciprocal of the square root of scan rate (from 5 to 10 V/s).

Effect of catalyst concentration

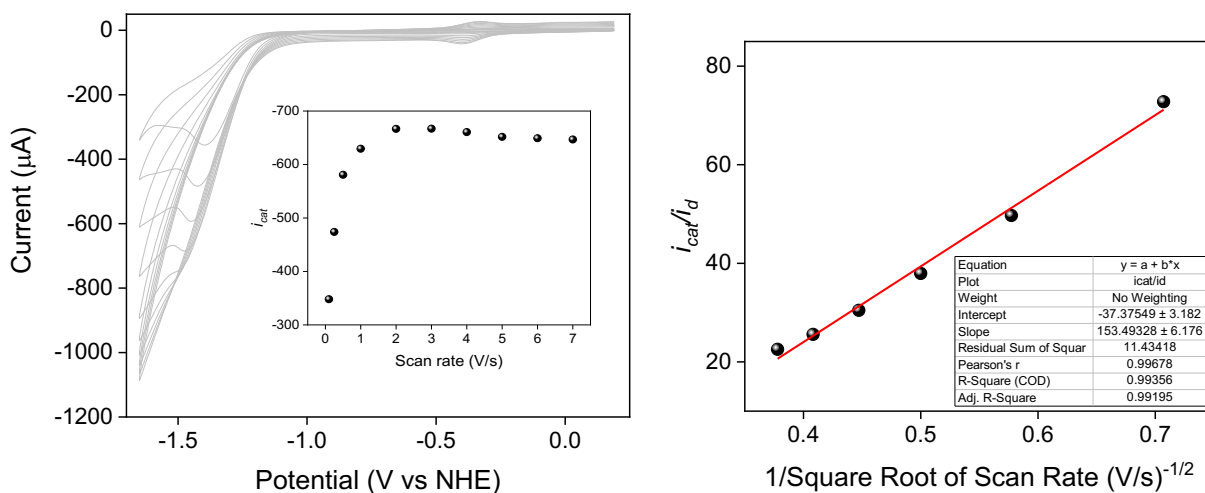


Figure S24. Right) CVs of **1** (100 μM) at various scan rates from 100 mV/s to 7 V/s in 0.1 M PBS at pH 7 under N_2 . Inset: plot of i_{cat} versus scan rate. b) Plot of i_{cat}/i_d versus the reciprocal of the square root of scan rate (from 2 to 7 V/s).

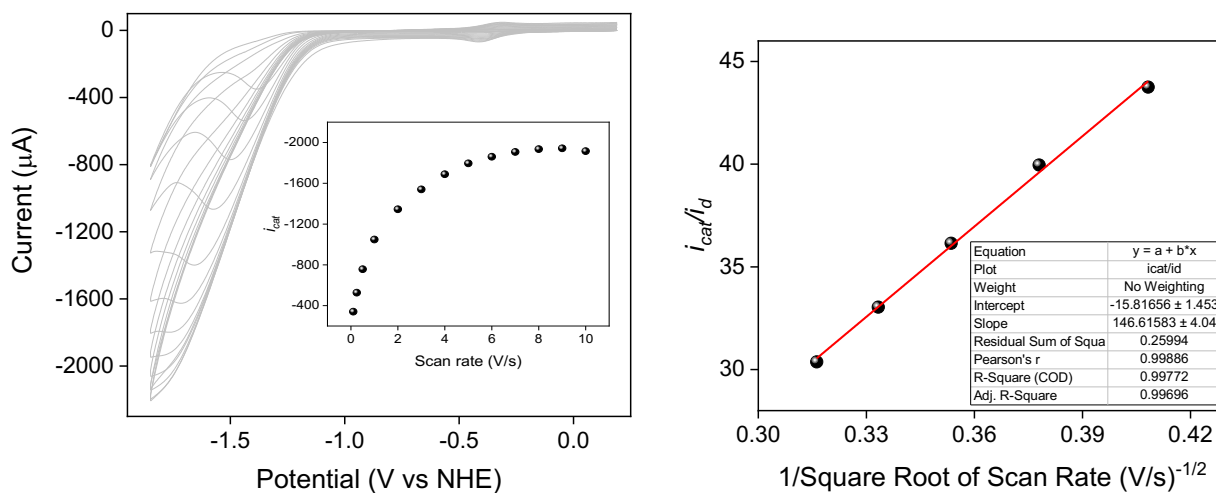


Figure S25. Right) CVs of **1** (200 μM) at various scan rates from 100 mV/s to 10 V/s in 0.1 M PBS at pH 7 under N_2 . Inset: plot of i_{cat} versus scan rate. b) Plot of i_{cat}/i_d versus the reciprocal of the square root of scan rate (from 6 to 10 V/s).

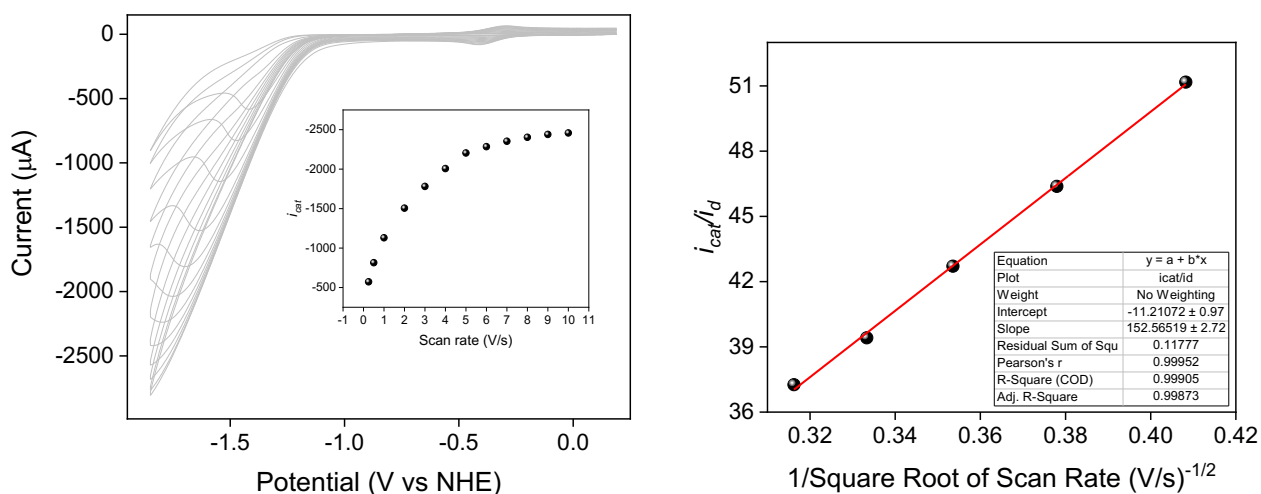


Figure S26. Right) CVs of **1** (350 μM) at various scan rates from 250 mV/s to 10 V/s in 0.1 M PBS at pH 7 under N_2 . Inset: plot of i_{cat} versus scan rate. b) Plot of i_{cat}/i_d versus the reciprocal of the square root of scan rate (from 6 to 10 V/s).

Effect of pH

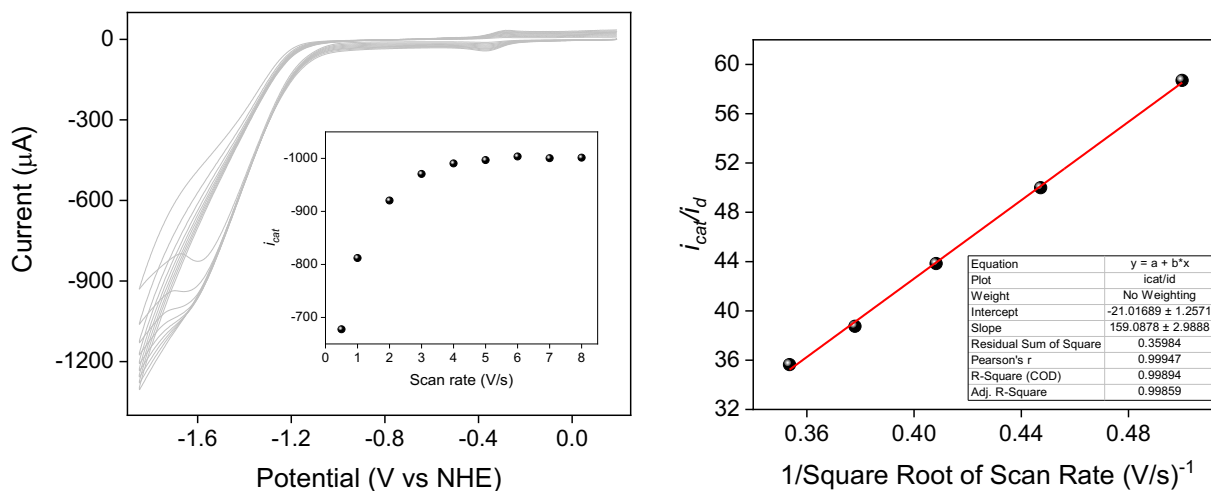


Figure S27. Right) CVs of **1** (200 μM) at various scan rates from 500 mV/s to 8 V/s in 0.1 M PBS at pH 5 under N₂. Inset: plot of i_{cat} versus scan rate. b) Plot of i_{cat}/i_d versus the reciprocal of the square root of scan rate (from 4 to 8 V/s).

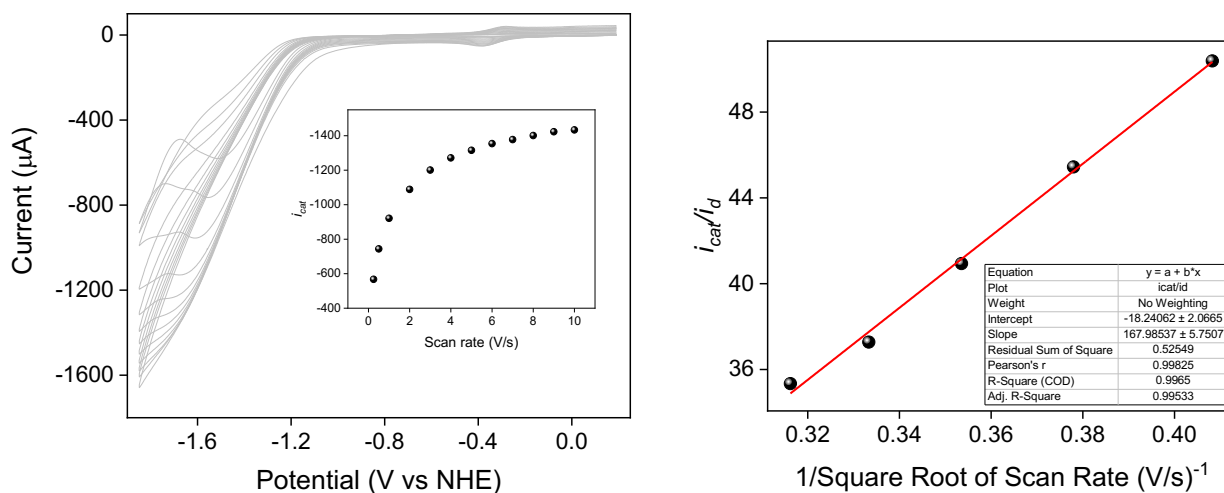


Figure S28. Right) CVs of **1** (200 μM) at various scan rates from 250 mV/s to 10 V/s in 0.1 M PBS at pH 6 under N₂. Inset: plot of i_{cat} versus scan rate. b) Plot of i_{cat}/i_d versus the reciprocal of the square root of scan rate (from 6 to 10 V/s).

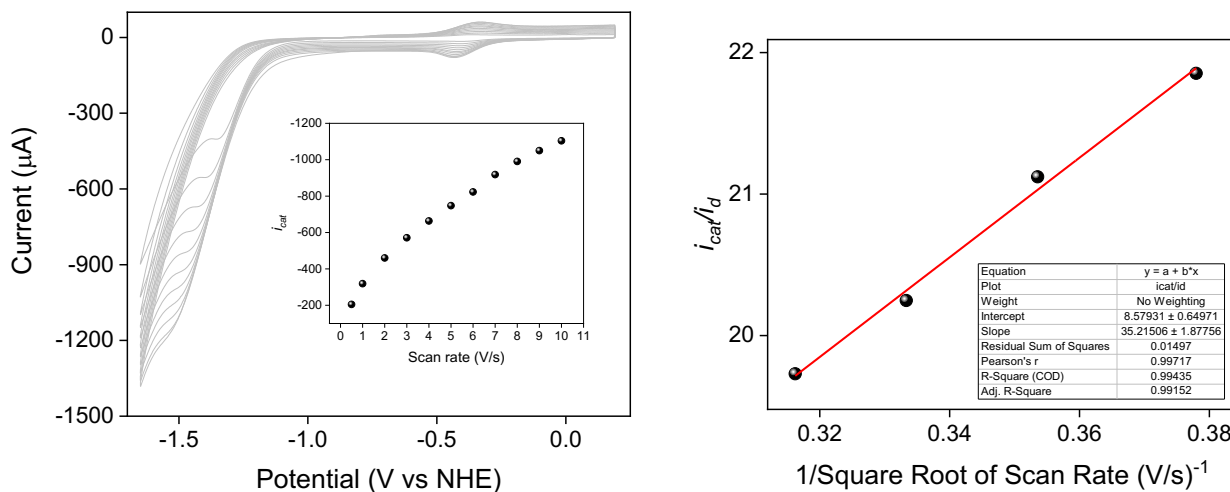


Figure S29. Right) CVs of **1** (200 μM) at various scan rates from 500 mV/s to 10 V/s in 0.1 M PBS at pH 8 under N_2 . Inset: plot of i_{cat} versus scan rate. b) Plot of i_{cat}/i_d versus the reciprocal of the square root of scan rate (from 7 to 10 V/s).

Effect of phosphate buffer concentration

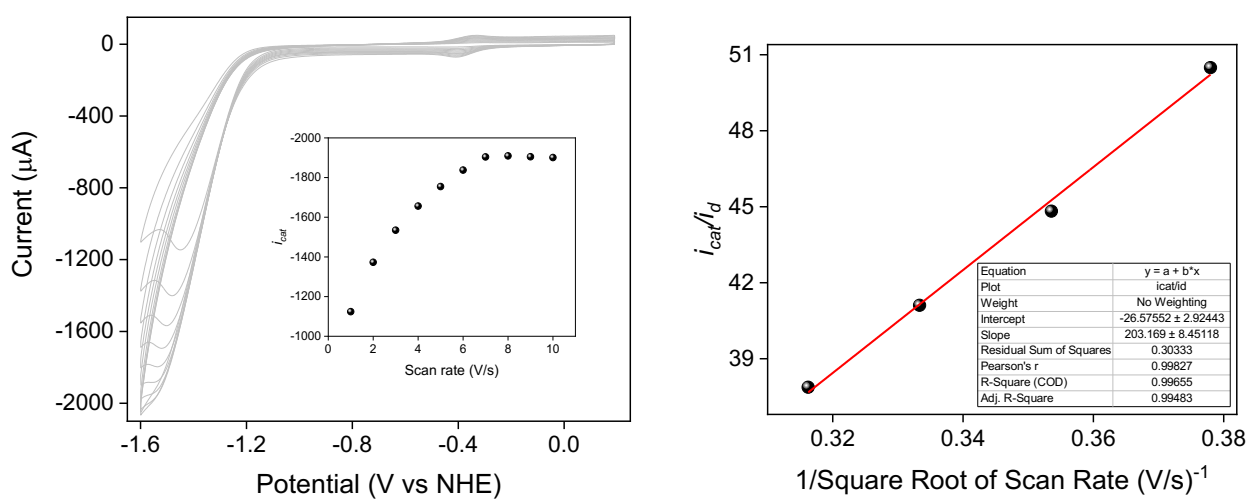


Figure S30. Right) CVs of **1** (200 μM) at various scan rates from 1 V/s to 10 V/s in 0.25 M PBS at pH 7 under N_2 . Inset: plot of i_{cat} versus scan rate. b) Plot of i_{cat}/i_d versus the reciprocal of the square root of scan rate (from 7 to 10 V/s).

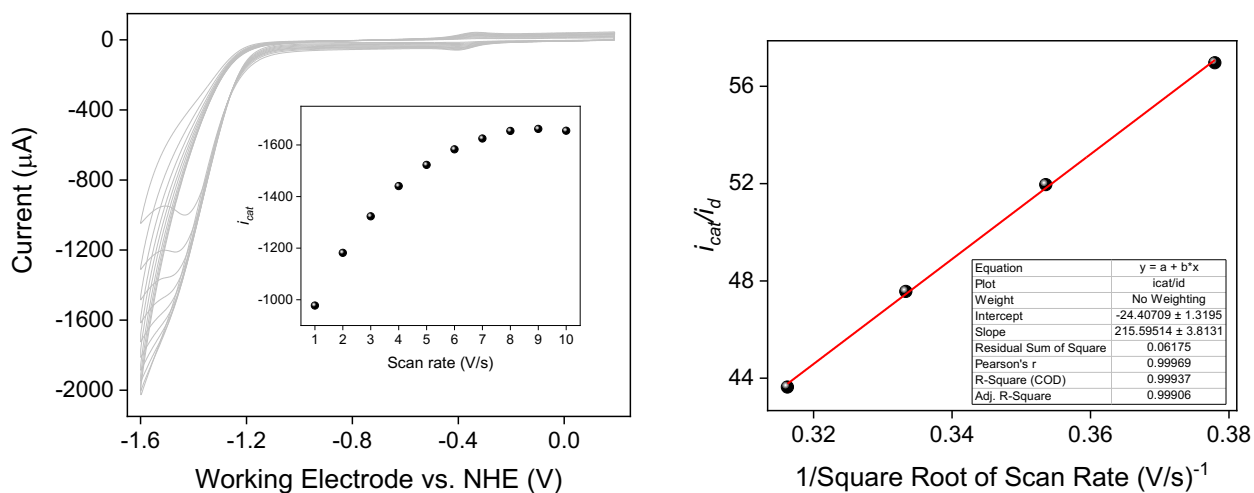


Figure S31. Right) CVs of **1** (200 μM) at various scan rates from 1 V/s to 10 V/s in 0.35 M PBS at pH 7 under N_2 . Inset: plot of i_{cat} versus scan rate. b) Plot of i_{cat}/i_d versus the reciprocal of the square root of scan rate (from 7 to 10 V/s).

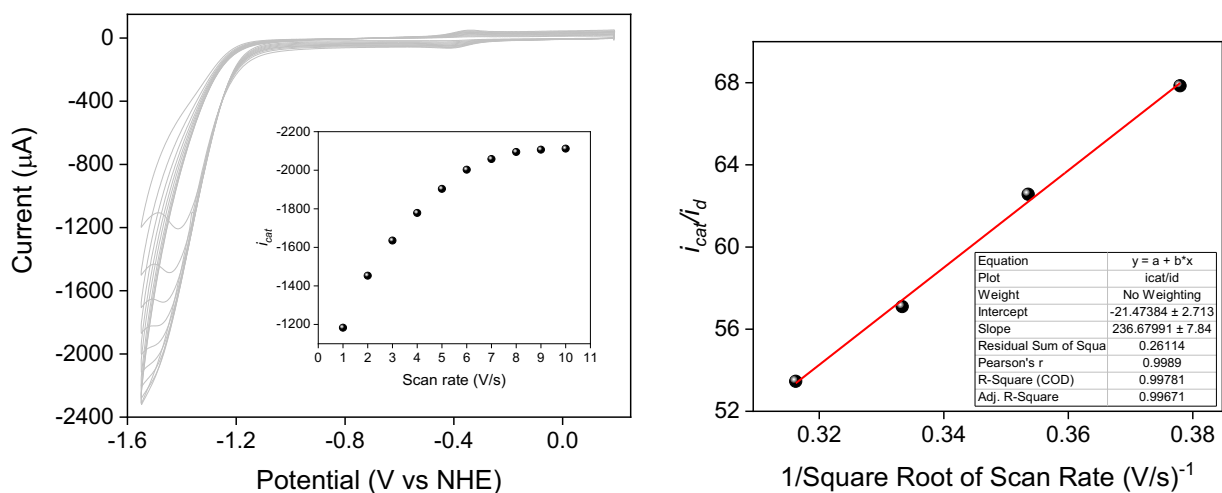


Figure S32. Right) CVs of **1** (200 μM) at various scan rates from 1 V/s to 10 V/s in 0.5 M PBS at pH 7 under N_2 . Inset: plot of i_{cat} versus scan rate. b) Plot of i_{cat}/i_d versus the reciprocal of the square root of scan rate (from 7 to 10 V/s).

III. DFT calculations

DFT calculations were carried out to investigate the catalytic mechanism for the HER. To understand the ligand effect on the catalytic performance, we selected complexes **1** and **3** as study cases since these complexes show drastically different catalytic properties. Specifically, while **1** shows an outstanding turnover frequency (TOF), consistently higher than **3**, the latter shows a lower overpotential (η). Our calculations provide a fundamental insight into chemical origin of such differences. The computed mechanism in aqueous solution at pH 7 and 298K is shown in Figure S32 for **1** (a) and **3** (b), respectively.

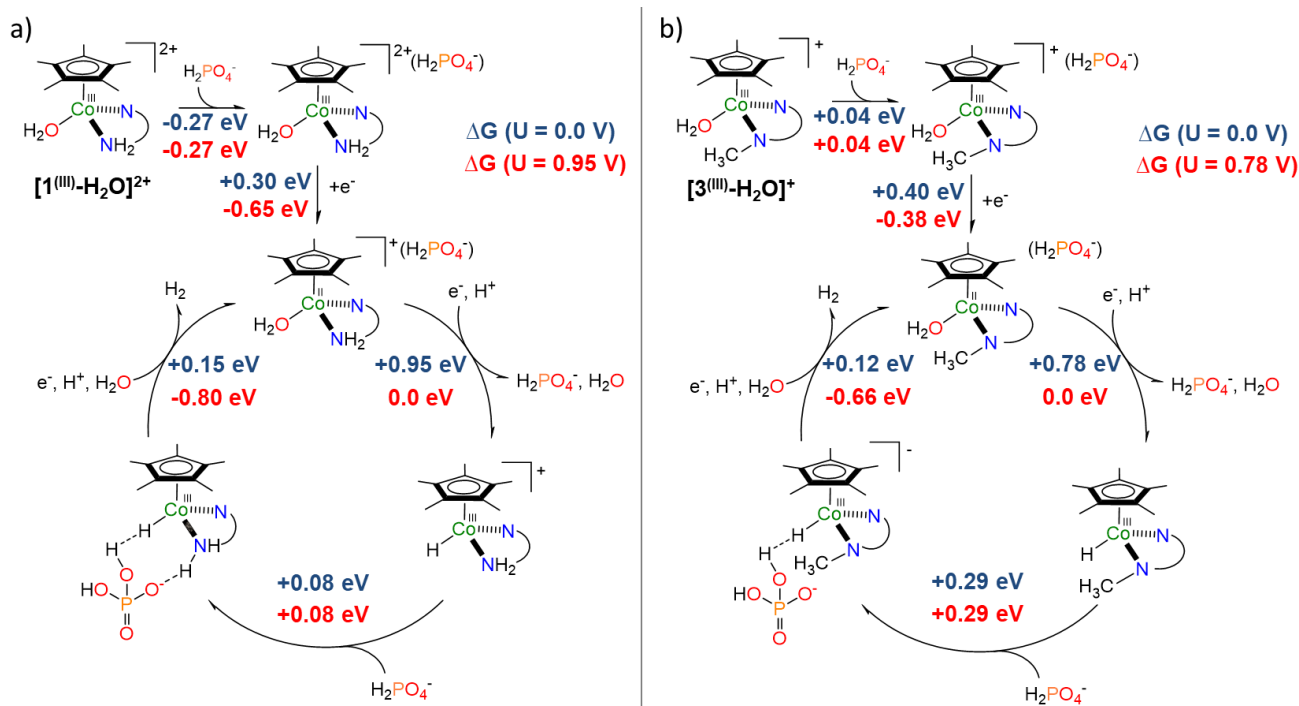


Figure S33. Proposed catalytic cycles for **1** (a) and **3** (b) and energetics at zero (blue) and onset (red) potentials.

In the following, we shall discuss the nature of the interaction between the catalyst and the buffer, the mechanism responsible for catalyst activation, the formation of the hydride complex (which is responsible for the measured overpotential), and the origin of the remarkable TOF experimentally measured. Emphasis is placed in discussing the role of the buffer and its role as proton relay.

The interaction between the catalyst and the buffer.

The use of a phosphate buffer solution leads to a significant increase of the experimental TOFs. A preliminary and fundamental question arises: is buffer coordination spontaneous at zero potential? If we consider the coordination of H_2PO_4^- in the second sphere (see Figure S32), the aggregation free energy is negative for **1** (-0.27 eV), indicating a spontaneous process. In contrast, a slightly positive aggregation free energy is shown for **3** ($+0.04 \text{ eV}$). To a large extent, this difference can be attributed to two effects:

- The higher positive charge of **1**, strengthening its interaction with the counteranion
- The presence of a hydrogen bond in **1** between the doubly protonated nitrogen in the amine group and the negatively charged oxygen of the phosphate.

It is worth mentioning that, for complex **1**, we also computed the water displacement reaction by H_2PO_4^- in the first coordination sphere. This process is favored by -0.41 eV . However, such coordination significantly increases the overpotential for the hydride formation ($+1.28 \text{ eV}$), indicating that the catalytically active species most likely feature the phosphate in the 2nd coordination sphere.

First reduction peak and catalyst activation

Experimentally, the $\text{Co}^{\text{III}} + e^- \rightarrow \text{Co}^{\text{II}}$ process requires 0.350 V for **1** and 0.345 V for **3**, as estimated from the first reduction peak in the CV. For **1**, we considered the complex with H_2PO_4^- in the second sphere, and the energy associated with the reduction process was found to be equal to 0.30 eV. For **3**, the phosphate-catalyst adduct with H_2PO_4^- in the second sphere is almost at equilibrium with the dissociated species, and hence the reduction potential was evaluated in both cases. It amounts to +0.40 eV for **3** with H_2PO_4^- in the second sphere and to +0.34 for the complex without H_2PO_4^- . The excellent agreement between theory and experiment is a further validation of the considerations made so far. Importantly, our calculations indicate that the actual catalyst of the transformation is the Co(II) complex that is formed at this stage, featuring the buffer in the second coordination sphere.

Metal-hydride complex formation and predicted overpotentials

The complex where a hydride is directly coordinated to the Cobalt is a crossroad for the hydrogen evolution reaction.^{9,10} Hence, two viable reaction paths starting from $[\mathbf{1}^{\text{(III)}}-\text{H}_2\text{O}]^+(\text{H}_2\text{PO}_4^-)$ (Figure S33a) and $[\mathbf{3}^{\text{(III)}}-\text{H}_2\text{O}](\text{H}_2\text{PO}_4^-)$ (Figure S33b) and leading to the hydride complex ($[\mathbf{1}^{\text{(III)}}-\text{H}]^+$ or $[\mathbf{3}^{\text{(III)}}-\text{H}]$, respectively) were considered. As shown in Figure S33, our calculations revealed that, for both **1** and **3**, the PCET exhibits a lower energy compared to the two-step reduction-protonation counterpart. Importantly, the calculated HER overpotentials for **1** and **3** amount to 0.54 eV and 0.38 eV, respectively.

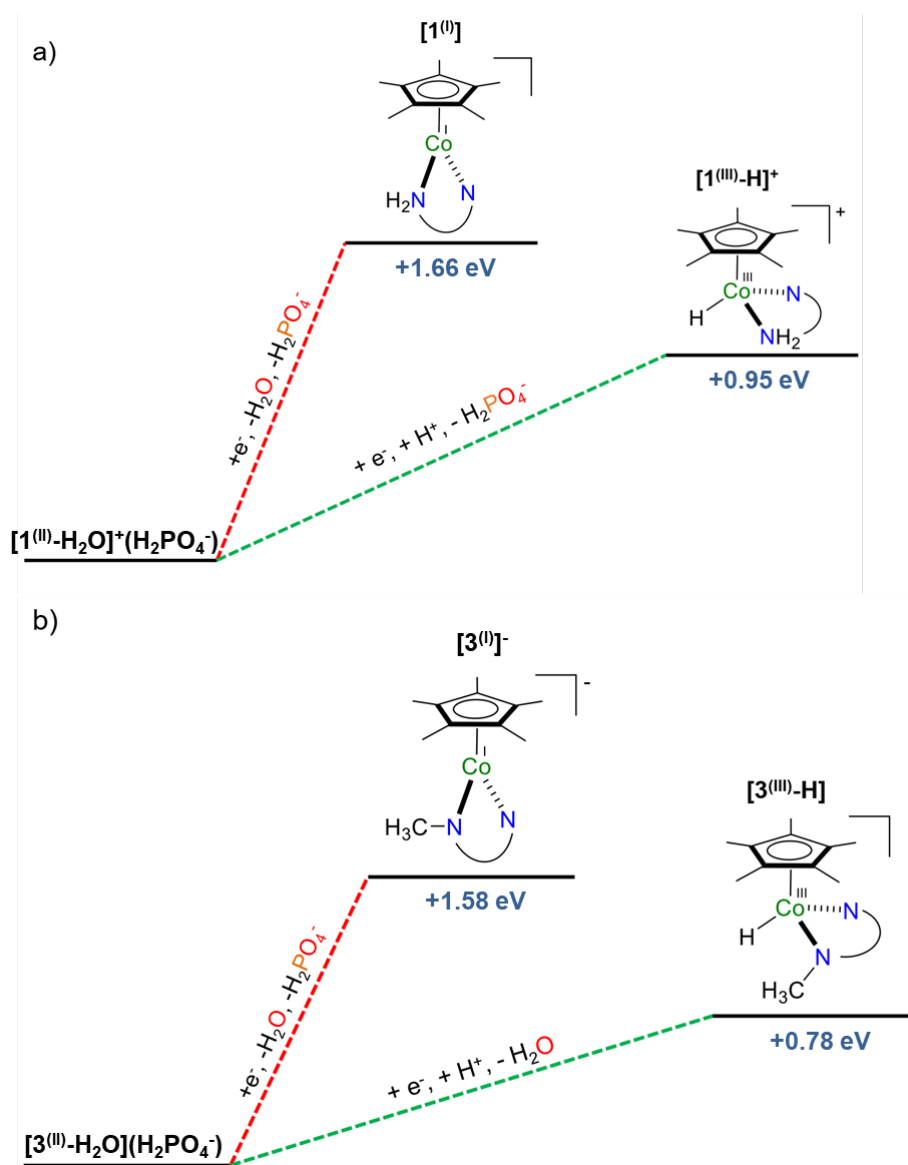


Figure S34. Calculated reaction pathways for the formation of the hydride complex of **1** (a) and **3** (b).

Hydrogen evolution and the origin of TOF

To explore the mechanism through which $H_2PO_4^-$ enhances the kinetics of HER, different reaction pathways for H_2 generation from $[1^{(III)}-H]^+$ and $[3^{(III)}-H]$ were computed. Direct reduction of $[1^{(III)}-H]^+$ and $[3^{(III)}-H]$ to form the corresponding Co(II) species requires 1.31 eV and 1.41 eV, respectively. These relatively high energy requirements hint at the possibility of a more energetically favourable concerted PCET process, eventually leading to the formation of H_2 . Indeed, our results revealed that the most favorable pathway for H_2 generation with both catalysts involves i) the coordination of $H_2PO_4^-$ in the second sphere of cobalt-hydride complex resulting in the formation of the key intermediates $[1^{(III)}-H]^+(H_2PO_4^-)$ or $[3^{(III)}-H](H_2PO_4^-)$ and ii) subsequent PCET process in which $H_2PO_4^-$ undergoes protonation to form H_3PO_4 while the catalyst is reduced (see Figure 34). Under these conditions, H-H bond formation becomes a barrierless process leading the release of H_2 and the

regeneration of the activated Co(II) species. Importantly, the calculated energy associated with the coordination of H_2PO_4^- to $[\mathbf{3}^{\text{III}}-\text{H}]$ in the second sphere was found to be equal to +0.29 eV, which is considerably higher than the +0.08 eV required for the formation of $[\mathbf{1}^{\text{III}}-\text{H}]^+(\text{H}_2\text{PO}_4^-)$. Hence, the origin of the markedly different TOFs of **1** and **3** can be ascribed to the tendency of H_2PO_4^- to be in proximity of the metal-hydride complex.

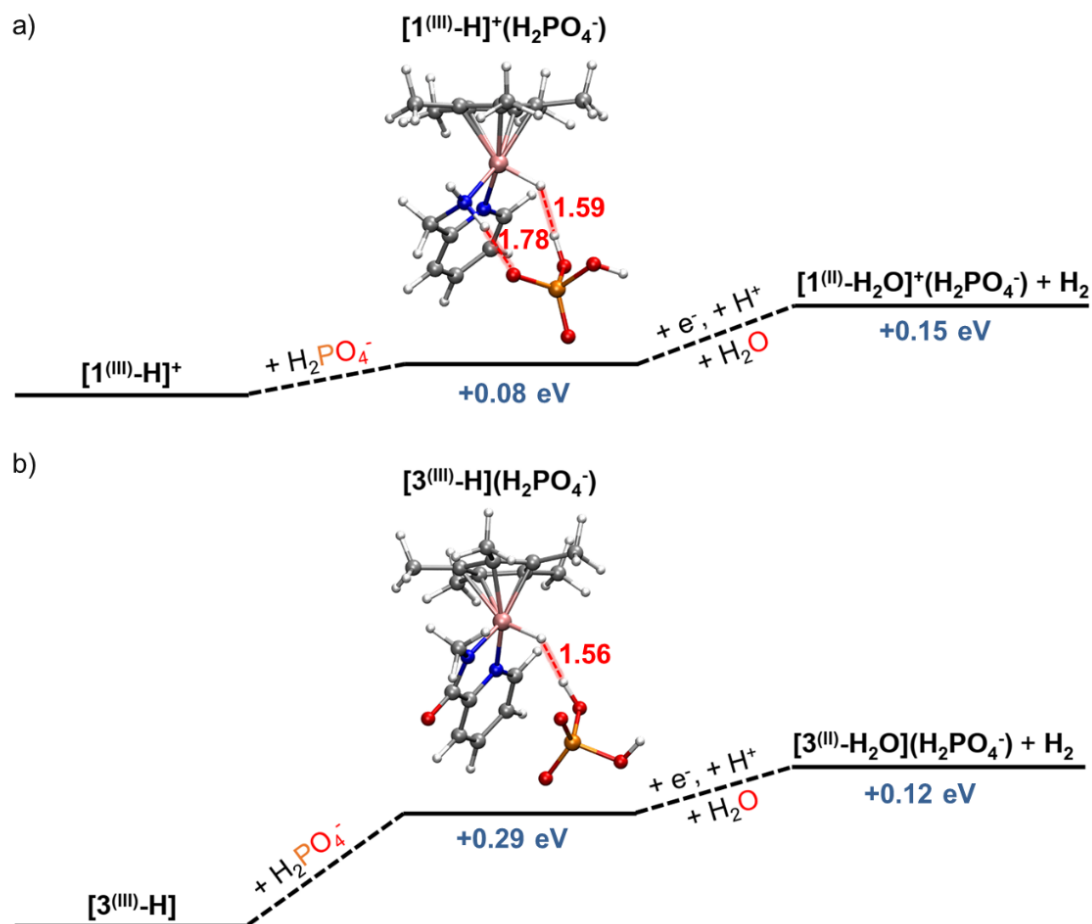


Figure S35. The calculated most favorable reaction pathway for the generation of hydrogen with **1** (a) and **3** (b) showing the optimized geometries of the key intermediates $[\mathbf{1}^{\text{III}}-\text{H}]^+(\text{H}_2\text{PO}_4^-)$ and $[\mathbf{3}^{\text{III}}-\text{H}](\text{H}_2\text{PO}_4^-)$. H-bond distances are reported in Å.

Computational details

All calculations were carried out using the ORCA quantum chemistry program package v 5.0.3.¹¹ Geometry optimizations were carried out using the B3LYP functional together with Grimme's D3 dispersion correction and Becke-Johnson damping.¹²⁻¹⁶ The Ahlrichs def2-TZVP(-f) basis set was used for all atoms.¹⁷ The water solvent was modeled using the C-PCM implicit solvation scheme.^{18,19} For each intermediate, all possible spin configurations were evaluated to identify the preferred reaction path. In Co(III) complexes, the metal center preferentially adopts a high-spin configuration, while lower Co oxidation states are associated with low-spin solutions. The minimum energy paths (MEP) for the H_2 bond formation mechanism were optimized using the nudged elastic band (NEB-

CI) method.^{20,21} Transition states were identified and characterized by a single imaginary frequency. All energies are reported with respect to the standard hydrogen electrode (SHE). In this work we used the IUPAC recommended value of -4.44 V.²² The value of -11.72 eV for hydration free energies of H⁺ was adopted.^{23,24} Additionally, a correction factor of $k_bT \times \text{pH} \times \ln 10 \approx 0.414$ eV was employed to consider in our calculations the H⁺ concentration in experimental conditions (10⁻⁷ M).

References

- 1 E. Higuchi, H. Uchida and M. Watanabe, *J. Electroanal. Chem.*, 2005, **583**, 69–76.
- 2 Y. Bao, K. Nagasawa, Y. Kuroda and S. Mitsushima, *Electrocatalysis*, 2020, **11**, 301–308.
- 3 J. G. Vos and M. T. M. Koper, *J. Electroanal. Chem.*, 2019, **850**, 113363.
- 4 J. Zheng, Y. Yan and B. Xu, *J. Electrochem. Soc.*, 2015, **162**, F1470–F1481.
- 5 D. H. Pool, M. P. Stewart, M. O'Hagan, W. J. Shaw, J. A. S. Roberts, R. M. Bullock and D. L. DuBois, *Proc. Natl. Acad. Sci. U. S. A.*, 2012, **109**, 15634–15639.
- 6 A. Dutta, S. Lense, J. Hou, M. H. Engelhard, J. A. S. Roberts and W. J. Shaw, *J. Am. Chem. Soc.*, 2013, **135**, 18490–18496.
- 7 C. P. Andrieux, J. M. Dumas-Bouchiat and J. M. Savéant, *J. Electroanal. Chem. Interfacial Electrochem.*, 1980, **113**, 1–18.
- 8 J. M. Saveant and E. Vianello, *Electrochim. Acta*, 1965, **10**, 905–920.
- 9 S. K. M. Padavala and K. A. Stoerzinger, *ACS Catal.*, 2023, **13**, 4544–4551.
- 10 Q. Wang, J. Guo and P. Chen, *Joule*, 2020, **4**, 705–709.
- 11 F. Neese and J. Wiley, *Wiley Interdiscip. Rev. Comput. Mol. Sci.*, 2012, **2**, 73–78.
- 12 A. D. Becke, *J. Chem. Phys.*, 1993, **98**, 1372–1377.
- 13 C. Lee, W. Yang and R. G. Parr, *Phys. Rev. B*, 1988, **37**, 785.
- 14 P. J. Stephens, F. J. Devlin, C. F. Chabalowski and M. J. Frisch, *J. Phys. Chem.*, 1994, **98**, 11623–11627.
- 15 S. Grimme, J. Antony, S. Ehrlich and H. Krieg, *J. Chem. Phys.*, , DOI:10.1063/1.3382344/926936.
- 16 S. Grimme, *Wiley Interdiscip. Rev. Comput. Mol. Sci.*, 2011, **1**, 211–228.
- 17 F. Weigend and R. Ahlrichs, *Phys. Chem. Chem. Phys.*, 2005, **7**, 3297–3305.
- 18 V. Barone and M. Cossi, *J. Phys. Chem. A*, 1998, **102**, 1995–2001.
- 19 M. Cossi, N. Rega, G. Scalmani and V. Barone, *J. Comput. Chem.*, 2003, **24**, 669–681.
- 20 G. Henkelman and H. Jónsson, *J. Chem. Phys.*, 2000, **113**, 9978–9985.
- 21 G. Henkelman, ; Blas, P. Uberuaga, H. Jónsson, B. P. Uberuaga and H. Jó, *J. Chem. Phys.*, 2000, **113**, 9901–9904.
- 22 S. Trasa'tti, *Pure Appl. Chem.*, 1986, **58**, 955–966.

- 23 I. A. Topol, G. J. Tawa, S. K. Burt and A. A. Rashin, *J. Chem. Phys.*, 1999, **111**, 10998–11014.
- 24 M. D. Tissandier, K. A. Cowen, W. Y. Feng, E. Gundlach, M. H. Cohen, A. D. Earhart, J. V. Coe and T. R. Tuttle, *J. Phys. Chem. A*, 1998, **102**, 7787–7794.